One-year-long turbulence measurements and modeling using large-eddy simulation domains in the Weather Research and Forecasting model

Peña, Alfredo; Mirocha, Jeffrey D.

Published in:
Applied Energy

Link to article, DOI:
10.1016/j.apenergy.2024.123069

Publication date:
2024

Document Version
Publisher's PDF, also known as Version of record

Applied Energy 363 (2024) 123069

Contents lists available at ScienceDirect

Applied Energy

journal homepage: www.elsevier.com/locate/apenergy

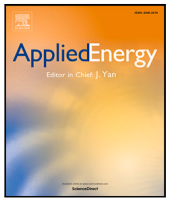

One-year-long turbulence measurements and modeling using large-eddy simulation domains in the Weather Research and Forecasting model

Alfredo Peña [a,*], Jeffrey D. Mirocha [b]

[a] DTU Wind and Energy Systems, Technical University of Denmark, Frederiksborgvej 399, Roskilde, 4000, Denmark
[b] Atmosphere, Earth and Energy Division, Lawrence Livermore National Laboratory, 7000 East Avenue, Livermore, 94550, United States

GRAPHICAL ABSTRACT

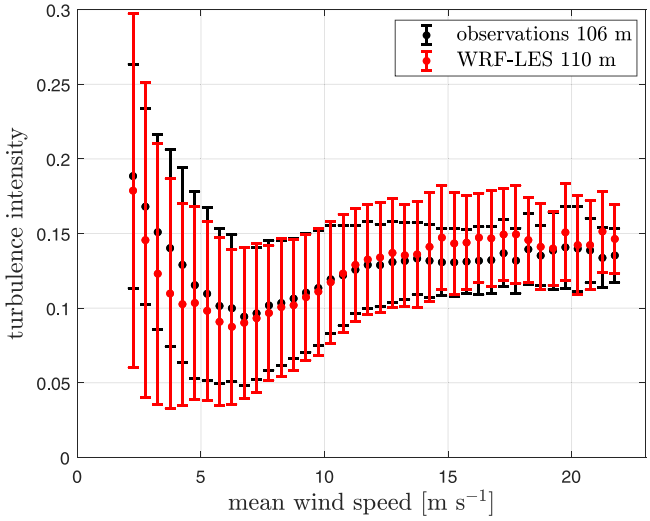

ARTICLE INFO

Dataset link: https://github.com/a2e-mmc/WRF, https://figshare.com/s/894bdb0cceb24c294b3c

Keywords:
Atmospheric turbulence
Large-eddy simulation
Mesoscale modeling
Site conditions
WRF

ABSTRACT

We present an intercomparison of a full year of turbulence measurements and simulations at Østerild, a site in northern Denmark with relatively flat terrain and high surface roughness, where a high-quality tall meteorological mast is deployed. Both sonic and cup anemometers are mounted on booms on the mast from 7 up to 244 m, thus covering the range of heights in which modern wind turbines operate. The simulations were performed using the Weather Research and Forecasting model in a multiscale setup, with large-eddy simulations (LESs) nested one-way within mesoscale simulations. The mesoscale domains thus simulated the evolving weather, while the two innermost domains used an LES closure, intending the largest scales of turbulence to be explicitly resolved. For a selected day, we show that the simulated turbulence is accurately resolved within the innermost LES domain, and agrees well with the observations at all vertical levels. For the full year, we show that the innermost domain accurately reproduces mean wind speed, direction, and turbulence levels, whereas the mesoscale simulations have difficulties matching the frequency of occurrence of both low and high turbulence ranges when compared to the observations. The largest differences between the simulated turbulence from the innermost domain and the observations are found under low wind speed

* Corresponding author.
E-mail address: aldi@dtu.dk (A. Peña).

https://doi.org/10.1016/j.apenergy.2024.123069
Received 8 August 2023; Received in revised form 14 March 2024; Accepted 18 March 2024
Available online 26 March 2024

conditions close to the surface, particularly during nighttime where the simulated mean wind and turbulence levels are higher and lower, respectively, than the observations, potentially due to the inability of the LES mesh to resolve the very small scales of turbulence and associated momentum transport that those features support.

1. Introduction

The use of atmospheric models to generate time series of the wind velocity components at different vertical levels, and over long time periods (e.g., for entire full years) is becoming increasingly common with the advent of affordable computation. These time series outputs are particularly useful for wind resource and energy yield assessments [1,2]. Long-term time series are typically represented by the instantaneous output of the atmospheric model, e.g., every 30 min or 1 h. This is because such outputs are computationally much less expensive and nearly as accurate, e.g., for mean wind speed and wind power density purposes, as those derived from constructing time series based on time-averages of model output over periods of, e.g., 10 or 30 min, as commonly performed with meteorological observations [3]. Further, most of these modeling systems are based on mesoscale simulations, an approach that can accurately capture the large-scale weather, but constrains the outputs to spatial and temporal scales of a several hundreds of meters to a few kilometers, and to tens of minutes, respectively, in the best of cases.

However, wind turbines as well as other structures such as buildings and bridges are designed to withstand specific site conditions, which are defined in the standards [e.g., 4]. An important part of these conditions involves measures of the levels of turbulence, which include processes that occur typically at high spatial resolutions (hundreds of meters at most) and at time scales of minutes to seconds. Turbulence has to be assessed as part of the site conditions because it directly affects the loads and performance of wind turbines [5]. However, in mesoscale simulations, turbulence cannot be explicitly resolved, and is therefore parameterized as a subgrid-scale (SGS) process. As such, turbulence derived from mesoscale simulations does not reliably provide the information required by the standards. Long-term time series of simulated turbulence measures could therefore offer to wind farm project developers, important information useful to select suitable machines that can withstand the turbulence conditions of the site. Further, they could also aid turbine manufacturers, in the design and optimization of wind turbines for particular turbulence conditions, sites and other operational considerations.

The Weather Research and Forecasting (WRF) model [6] is a commonly used atmospheric model, which is typically utilized to simulate mesoscale weather. This is achieved by downscaling the output from global-scale numerical weather prediction models to spatial scales of tens to a few kilometers, at which relevant smaller-scale weather features can be represented. However, mesoscale domains still use meshes that are too coarse to capture atmospheric turbulence directly. Instead, mesoscale simulations rely upon one-dimensional planetary boundary layer (PBL) schemes to parameterize the turbulent fluxes of heat, momentum, and other constituents, in the vertical direction only, within the atmospheric boundary layer. While some mesoscale PBL schemes include a variable to represent SGS turbulence kinetic energy (TKE), this is a parameterized quantity, which might not capture the fine turbulence details.

To enable the direct simulation of turbulence motions, the WRF model (and other mesoscale simulation codes) support refinement of the mesh to scales capable of resolving the important scales of atmospheric turbulence directly. For this purpose, a number of additional SGS models designed for LES have been implemented into the WRF model [7,8]. This approach is hereafter refereed to as WRF-LES. These models allow for the explicit representation of the energetically important scales of atmospheric turbulence, while accounting for the effects of unresolved small-scale fluctuations on those resolved-scale motions. Therefore, using PBL schemes on mesoscale domains, and switching to LES SGS models once the mesh spacing is sufficiently fine to resolve turbulence motions explicitly, provides a methodology for the explicit simulation of turbulence motions occurring within mesoscale simulations, as well as for additional improvements in fidelity from additional fine-scale forcing, such as terrain or surface cover variability. WRF-LES has been applied previously to wind energy case studies involving a diurnal cycle over simple terrain [9], stable and convective conditions over complex terrain [10], and during a mesoscale frontal passage [11], in each case showing very good agreement with observations in both mean and turbulence quantities. WRF-LES was also used to study the development of an atmospheric hydraulic jump and mountain waves, which were observed with long-range scanning lidars [12]. Idealized simulations using the WRF model also employed an LES approach to study atmospheric turbulence under different atmospheric stability conditions [13] and to assess the fidelity of mesoscale wind-farm parametrizations by comparison with high resolution LES of wind turbine wakes [14]

Here, we show results of analysis of a full year of atmospheric simulations performed with a WRF-LES-based modeling system, with the goal of describing both the mean wind as well as the turbulence characteristics at a specific site. The site is Østerild, located in northern Jutland, Denmark, which features relatively flat terrain, but with heterogeneous and seasonally varying surface roughness, and where high-quality observations of wind and turbulence are available from instruments deployed at several vertical levels on a 250-m tall meteorological mast, thus covering the range of heights within which modern wind turbines operate. From the author's knowledge, this is one of the first studies showing the ability of atmospheric modeling systems to resolve and model turbulence with these details for this relatively long period, which can provide the necessary output for the assessment of the turbulence-related site conditions of wind turbines. Schalkwijk et al. [15] was perhaps the first study showing the advantages of using LES (based on the Dutch Atmospheric Large-Eddy Simulation model) to study atmospheric flow within a broad range of scales for an entire year. However, that study used coarser horizontal resolution and focused substantially on temperature, moisture, and clouds, while the present study uses finer resolution and focuses on wind resources. In Section 2, we introduce the Østerild site and the measurements from the mast. Section 3 provides the details of the numerical setup and the simulations. In Section 4, we provide the results both for a selected day (Section 4.1) and for the full year (Section 4.2). Section 4.3 illustrates results of a sensitivity analysis on different alternatives to instigate turbulence in the boundaries of the LES domains. The two last sections contain a discussion and conclusions of the study.

2. Site and measurements

Measurements from the entire 2017 were collected from instruments installed on a mast, which is deployed at the Østerild test station for large wind turbines in northern Denmark. Østerild is located on a land area between the North Sea and the Limfjorden waters (see Fig. 1). At Østerild, the terrain is flat and heterogeneous from a combination of agricultural and cropland, forest, and urban areas. North of the mast, there were only seven test stands for wind turbines; nowadays there are two more test stands south of the mast.

We use measurements from RisøP2546 A cup anemometers at 10, 40, 70, 106, 140, 178, 210, and 244 m above the ground (agl; to which hereafter all heights are referred) and Metek USA-1 sonic anemometers

Table 1
Model setup for the numerical simulations.

Domain	Δx [m]	Nest ratio	$N_x \times N_y$	Δt [s]	PBL scheme/turbulence closure
d01	6250	–	202 × 202	37.5	MYNN2
d02	1250	5	201 × 201	7.5	MYNN2
d03	250	5	201 × 201	1.5	TKE 1.5
d04	50	5	201 × 201	0.3	TKE 1.5

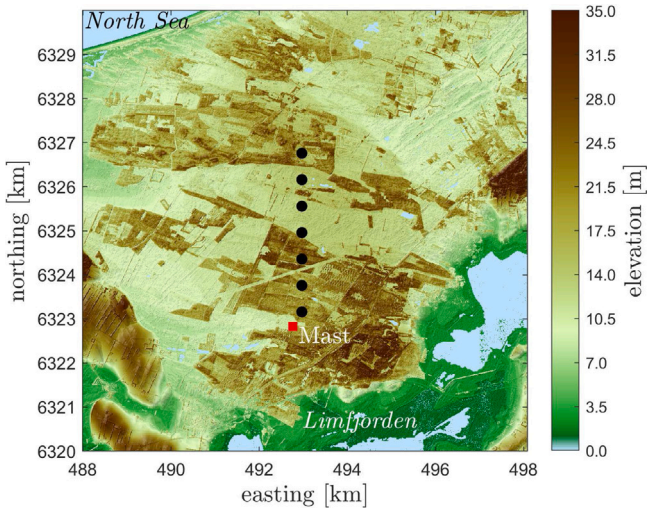

Fig. 1. The Østerild test station and surrounding area in northern Jutland, Denmark on a digital surface model (UTM WGS84) from 2017. Turbine locations are shown in black circles and the meteorological mast in the red rectangle.

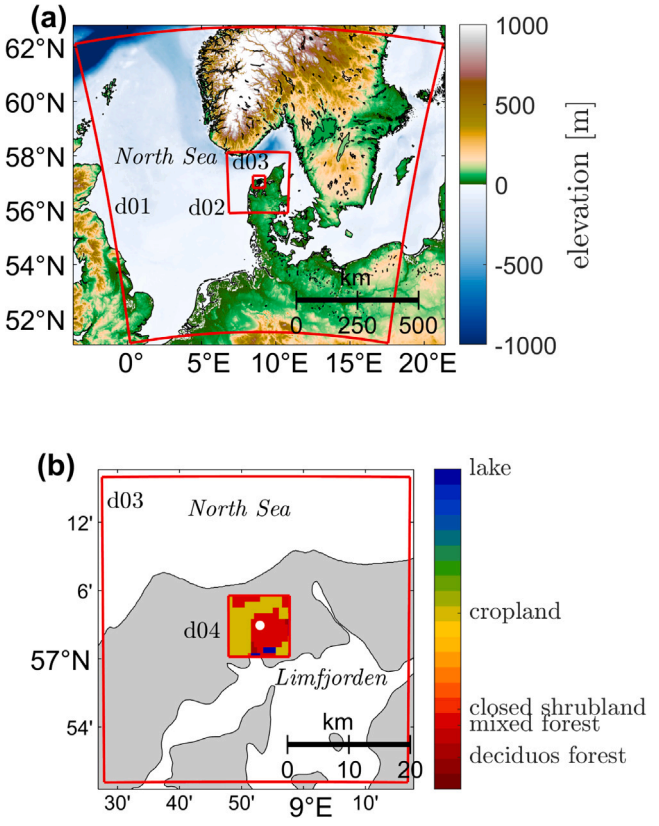

Fig. 2. (a) Telescopic nested domains d01–4 (red solid lines) used for the WRF model simulations. All domains are centered on the Østerild meteorological mast in Denmark. (b) Land cover of the innermost domain (d04) from the US Geological Survey classification with the Østerild mast shown in white.

at 7, 37, 103, 175, and 241 m. We also use measurements from the reference wind vanes at 40 and 244 m. When sonic anemometer measurements are utilized, we remove the instrument's default flow distortion 2D correction and apply the 3D correction suggested by GmbH [16]. The latter corrects the velocity components so that their spectra show the inertial subrange ratio of 4/3 as expected from Kolmogorov's hypothesis [17]. Other details about the area and the measurements are provided in Peña [18].

3. Numerical simulations

We perform real-time multiscale atmospheric simulations using the WRF model (version 4.1.2), which is a non-hydrostatic, fully compressible solver of the Euler equations. We use the horizontal grid nesting capability of the WRF model to concurrently simulate the atmosphere over four one-way nested domains, which are all centered at the position of the Østerild meteorological mast (see Fig. 2a). In the WRF model, horizontal grid nesting can be achieved by proving lateral boundary conditions from a coarser domain to a finer grid domain at each time step of the coarser grid [6].

Starting from the outermost (d01) down to the innermost (d04) domain, the horizontal grid spacing of the domains (Δx) is 6250, 1250, 250, and 50 m. All domains have nearly the same amount of grid points in both horizontal directions ($N_x \times N_y = 201 \times 201$). All domains have 61 vertical levels with the model top boundary at 5000 Pa. The first 20 vertical levels are within the first kilometer from the model bottom; 10 vertical levels are within the first 250 m covering the mast (at ≈11, 32, 48, 65, 81, 100, 125, 154, 186, and 223 m). Table 1 presents a summary of the model domains' specifications.

We use the ERA5 reanalysis at 0.3° [19] to initialize and force the model outermost domain. Additional boundary conditions come from the Operational Sea Surface Temperature and Sea Ice Analysis [20]. The WRF-default land cover and terrain elevation datasets are used as inputs: Moderate Resolution Imaging Spectroradiometer (MODIS) land cover classification and global multiresolution terrain elevation data 2010 at 30 arcsec [21]. Fig. 2b illustrates the land use of the innermost domain together with the position of the Østerild mast. The WRF-default land cover depicts Østerild as mixed forest surrounded by cropland. Although details are missing, the land use description used in the model fits the area well and this will be reflected when analyzing the simulations below.

The timestep (Δt) used for the outermost domain is 37.5 s and with a 1:5 timestep ratio between domains, that of the innermost domain is 0.3 s. The following physical parameterizations are selected for the mesoscale domains: the single moment 5-class scheme for cloud microphysics [22], the Kain–Fritsch scheme for cumulus convection [23] at a 5-min frequency, and only applied to the outermost domain, and the MYNN level-2.5 (MYNN2) planetary boundary layer (PBL) scheme [24] (PBL domains hereafter). This PBL scheme uses a QKE-based prognostic equation to model TKE; QKE corresponds to twice the TKE. This subgrid TKE should not be confused with the TKE from the subgrid model of LES; hereafter we refer to the former and latter as e and e_{sgs}, respectively, to differentiate between them.

The standard WRF model does not have an explicit low-pass filter but it is the grid and numerics that implicitly filter the fields. For the simulation of the innermost domains (run in LES mode), we use the standard WRF SGS stress model of Deardorff [25], which utilizes a eddy-viscosity approach of the form:

$$\tau_{ij} = -2\nu_T \tilde{S}_{ij}, \tag{1}$$

where $\tilde{S}_{ij}$ is the resolved strain-rate tensor, and ν_T is the eddy-viscosity coefficient assumed as

$$\nu_T = C_e l \sqrt{e_{\text{sgs}}}, \tag{2}$$

where $C_e = 0.15$, $l = (\Delta x \Delta y \Delta z)^{1/3}$, and e_{sgs} is the SGS TKE, which is computed from a TKE-based prognostic equation similar to that employed by the MYNN2 PBL scheme. All domains employ the MYNN surface-layer scheme [24] and the Unified Noah Land Surface model [26]. For shortwave and longwave radiation, all domains use the RRTMG scheme [27] at a 6-min frequency.

Simulations are performed for the entire year of 2017 for all domains through 37 simultaneous, parallel 10-day-long runs, each with a spinup of 12 h. Such spinup time was found to provide balance between the large-scale flow, the model physical parameterizations, and the surface forcing when simulating within regions with similar climatology [28]. From the 37 10-day-long runs, two experience numerical instabilities and require a reduction of the model timestep. In these cases, $\Delta t = 20$ s is used for the outermost domain. Spectral nudging towards the forcing reanalysis is utilized for the two horizontal wind components and temperature on the outermost domain with a constant of 0.0003 s^{-1} [29]. No upper level damping was used. Two-dimensional deformation and second-order diffusion are used for the PBL domains, while three-dimensional turbulence mixing in physical space is used for the LES domains [6]. Sixth-order positive definite numerical diffusion [30] as well as positive definite advection of moisture and scalars are used for all domains.

Due to the high computational cost of processing these multiple-domain simulations, we extract the output of the simulations from each of the domains at the grid point closest to the Østerild mast only. For domains other than the innermost LES domain (d04), the output is instantaneous and produced hourly, except for one particular day that we study in detail, where the instantaneous output is every 10 min. For the innermost LES domain, instantaneous output from the simulation is produced every 12 s. Each 10-day-long run (including spinup) was performed on 10 32-core nodes on the Sophia cluster [31] and took 120 h to complete.

When performing multiscale simulations with the WRF model, three-dimensional turbulence within the nested LES domains can be slow to develop, due to the lack of resolved turbulence features contained within the bounding-domain solution, which contains insufficient mesh spacing, and uses a one-dimensional PBL scheme that is not designed to resolve turbulence. The formation of turbulence is therefore accelerated by applying the stochastic cell perturbation method (CPM) [32,33] at the inflow boundaries of the LES domains. The CPM is configured in the standard manner, using perturbation zones of three perturbation cells, each consisting of eight by one grid cells in the horizontal and vertical directions, respectively (see Fig. 3). The magnitude of the perturbations are chosen to satisfy the optimal turbulent Eckert number (0.2), which spurs the development of hairpin-like vortices that quickly grow to form a realistic three-dimensional turbulence field [32].

Since our simulation spans an entire year, the standard CPM methodology of Muñoz-Esparza and Kosović [33], which requires performing a mesoscale simulation first to determine the CPM parameters, and then reading those parameters in during a subsequent multiscale simulation with the nested LESs, is impractical. Instead, the CPM used herein runs concurrently within the multiscale simulation, with the required control parameters passed down from the mesoscale domain and its PBL parameterization on d02 during execution. One

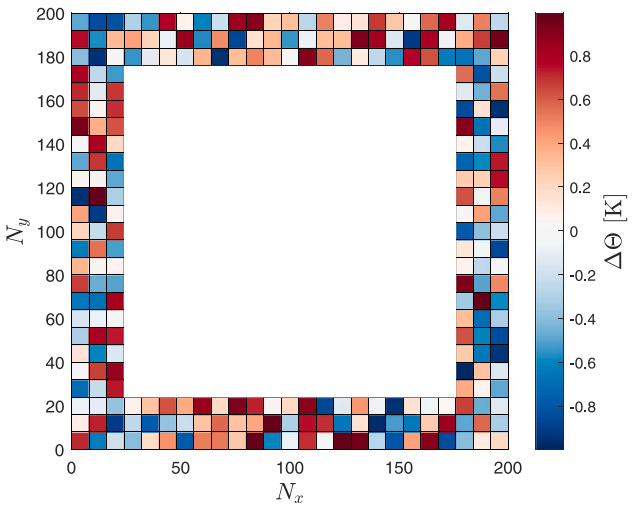

Fig. 3. Illustration of the cell perturbation method applied to the boundaries of an LES domain with 3 horizontal cells with random potential temperature amplitudes $\Delta\Theta \pm 1$ K.

key parameter is the PBL height, which is used to specify both the depth to apply the perturbations, as well as the perturbation amplitude. The perturbation amplitude, which is computed from the turbulent Eckert number, requires the geostrophic wind speed, the value of which is approximated by the average horizontal wind speed computed at a vertical level that is 10% higher than the maximum PBL height occurring within the outer mesoscale domain. The perturbations are then applied up to 80% of the PBL height. Another parameter that is adjusted in real time is which lateral boundaries to perturb, determined by the direction of the mean geostrophic wind, with perturbations applied along boundaries with flow oriented into the domain. Finally, the time interval over which to reapply the perturbations is determined using the advective timescale of the perturbation zone, here taken to be 85% of the 24 grid cells perturbed, with the slight reduction accounting for the relaxation zone of 5 grid cells adjacent to each lateral boundary, over which the flow variables within a nested domain are linearly blended with their respective parent-domain values. We assume that this relaxation shortens the effective perturbation zone by one half of the width of the relaxation zone. The advective time scale is then computed as the time to span the adjusted perturbation zone using the average wind speed at the height of the cells being perturbed. An additional adjustment is made to lengthen the timescale by up to a factor of the square root of two, based on the angle of the flow relative to the computational mesh.

4. Results

For a selected day, which we present in Section 4.1, we resample (not average) the 20-Hz sonic anemometer data to 12 s for direct comparison with the 12-s output of the innermost LES domain (d04). We also compute 10-min statistics based on the 20-Hz sonic anemometer data. We compare these statistics with the simulations' 10-min instantaneous output of all domains except for the innermost LES domain (d04). For the latter domain, we use both the 12-s output directly and also compute the corresponding 10-min statistics from the 12-s output. For the entire full year intercomparison (Section 4.2), we compute 10-min statistics based on the 1-Hz cup anemometer data, 10-min statistics from the 12-s output of the simulation of the innermost LES domain, and use the instantaneous hourly output of all other domains. All time references are based on Danish standard time (UTC+1).

Cup anemometers measure the horizontal velocity magnitude U, which can also be obtained from the two horizontal velocity components measured from the sonic anemometers. On a Cartesian coordinate

system:

$$U = \left(u_x^2 + u_y^2\right)^{1/2}, \tag{3}$$

where u_x and u_y can be, e.g., the zonal and meridional components of the wind. The cup anemometer velocity variance $\langle U'U' \rangle$, where the prime denotes fluctuation from the mean, which is here denoted within $\langle\rangle$ and represented as a time average within a 10-min period in our analysis, but more precisely its root square, is used to estimate the turbulence intensity (TI) as

$$\mathrm{TI} = \frac{\sqrt{\langle U'U' \rangle}}{U}, \tag{4}$$

which is, e.g., a key parameter for site selection of suitable wind turbines.

The 20-Hz sonic anemometer observations and the 12-s output from the simulations of the innermost LES domain are similarly analyzed. Within each 10-min interval and for each vertical level, the sonic anemometer velocity components are rotated so that the u-velocity component (the along-wind component) becomes aligned with the 10-min mean wind, i.e., $\langle u \rangle = \langle U \rangle$. Thus, the v-velocity component becomes the cross-wind component with w being the vertical velocity component. In this way, the variance of the horizontal velocity measured by a cup anemometer is very close to that estimated from the along-wind component, which can be derived from a sonic anemometer, i.e., $\langle U'U' \rangle \approx \langle u'u' \rangle$.

For the innermost LES domain (d04), we chose to output the instantaneous zonal, meridional, and vertical velocity components, e_{sgs}, and the deviatoric part of the subgrid stresses $\tau_{ij}^{\mathrm{dev}} = \tau_{ij} - \tau_{kk}\delta_{ij}/3$. From the 12-s output of d04, we first estimate the magnitude of the horizontal velocity, the flow direction, and the SGS stresses. The latter are

$$\tau_{ij}^{\mathrm{sgs}} = (2/3)\delta_{ij} e_{\mathrm{sgs}} + \tau_{ij}^{\mathrm{dev}}, \tag{5}$$

without implicit summation. Then, within each 10-min interval, we compute both the mean horizontal velocity and mean wind direction (from the mean zonal and meridional simulated winds), and the resolved stresses

$$\tau_{ij}^{\mathrm{res}} = -\rho \langle u_i' u_j' \rangle, \tag{6}$$

where ρ is the air density. The total stress components are computed as

$$\tau_{ij}^{\mathrm{tot}} = \tau_{ij}^{\mathrm{res}} + \langle \tau_{ij}^{\mathrm{sgs}} \rangle, \tag{7}$$

which are then rotated to the mean wind as $\tau_{ij} = a_{im} a_{jn} \tau_{mn}^{\mathrm{tot}}$, where a_{ij} are the components of the rotation matrix. This procedure is performed at each simulated vertical level.

4.1. Selected day

We select a day, June 12, 2017, to explore the capabilities of WRF-LES in detail. This particular day is selected because it shows a wide range of wind speeds within the operational envelope of wind turbines and winds are from the predominant wind direction (west) most of the day (see Figs. 4 and 6). We show first for three vertical levels covering the extension of the mast, the variability of the 12-s WRF-LES output for the horizontal velocity and that of the resampled observations from the sonic anemometers (Fig. 4).

As illustrated, both the sonic anemometer and WRF-LES high-frequency time series follow the same trends at these three vertical levels. Differences between the simulations and observations are more clearly visible the closer to the ground. At 7 m, the simulated winds tend to be larger than the observations during the morning and the opposite occurs during the afternoon. This bias often occurs close to the surface because the vertical shear is overestimated by LES [34]. This behavior becomes less discernible with increasing distance above the ground, and by 241 m is no longer detectable. The variability

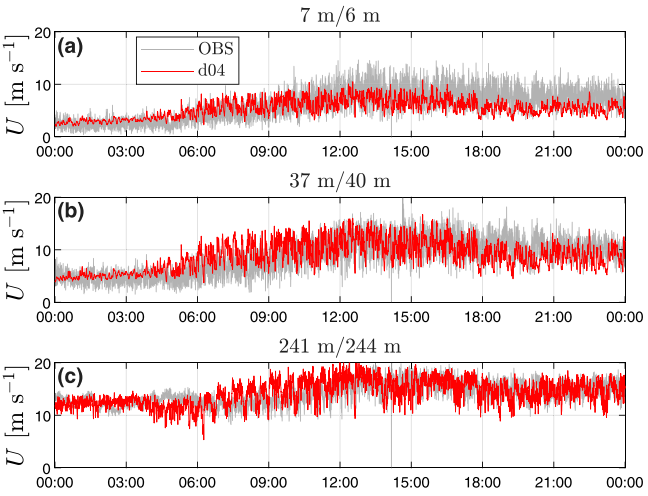

Fig. 4. Time series of horizontal velocity from 12-s resampled sonic anemometer observations (OBS) and 12-s output from the innermost LES domain (d04) at three different observational heights: 7, 37, and 241 m in panels (a), (b), and (c), respectively, at Østerild. For the simulated winds, the closest vertical levels to the observations are at ≈6, 40, and 244 m.

in the fluctuations of the WRF-LES output similarly shows improving agreement with the observations with increasing distance above the ground. This behavior is well portrayed by the horizontal velocity histograms in Fig. 5, which were constructed based on the high-frequency time series of both observations and simulations at the same three vertical levels. One can notice that the 6-m simulated winds exhibit less fluctuations than those at higher levels due to poorly resolved scales close to the surface: the daily variance of the 6-m simulated wind is 2.74 $\mathrm{m^2\ s^{-2}}$, whereas that of the 40- and 244-m winds are 7.24 and 5.65 $\mathrm{m^2\ s^{-2}}$, respectively. Also, all simulated winds fluctuate less in the early morning hours than in the rest of the day: at 6-m, the variance of the simulated wind is 0.18 $\mathrm{m^2\ s^{-2}}$ within 00:00–03:00 and 1.65 $\mathrm{m^2\ s^{-2}}$ within 12:00–15:00, whereas the variance of the observed winds is 0.72 and 5.04 $\mathrm{m^2\ s^{-2}}$ within the same two periods, respectively. At 37 m and within 12:00–15:00, the variance of the simulated and observed wind is 4.58 and 6.61 $\mathrm{m^2\ s^{-2}}$, respectively, whereas within the same period but at 241 m, it is 4.60 and 3.31 $\mathrm{m^2\ s^{-2}}$, respectively. Note that this particular day belongs to one of the 10-day simulations used for the year-long analysis; this particular simulation starts on June 10, 2017.

In Fig. 6, we notice the effect of the fluctuating simulated horizontal velocity components on the high-frequency time series of wind direction, the simulations following closely the trend of the sonic anemometer observations for two vertical levels. As expected from the findings in Fig. 4, the simulations capture more closely the variability of the observed winds the farther from the ground. Although there is reduced variability in the simulations compared to the observations, specially in the early morning hours, for this particular day, the simulations capture the large vertical wind veer between the 241- and 37-m sonic anemometers: at 01:30 the simulated instantaneous wind veer and the sonic-derived mean wind veer are 14.52° and 13.68°, respectively.

Fig. 7 also shows time series, but at a 10-min frequency, of the winds for the selected day but we include the instantaneous output of the two mesoscale domains (d01 and d02) and the other LES domain (d03). Also for both wind speed and direction, we show the 10-min mean from the output of the innermost LES domain (d04) and the 10-min mean from the cup anemometer observations. Here, we focus on the 110-m height, since this is a common hub height of modern and large wind turbines.

All domains follow the observed winds closely (Fig. 7a), although the two outermost mesoscale domains (d01 and d02) slightly overpredict the wind speed during the early morning. As expected, the

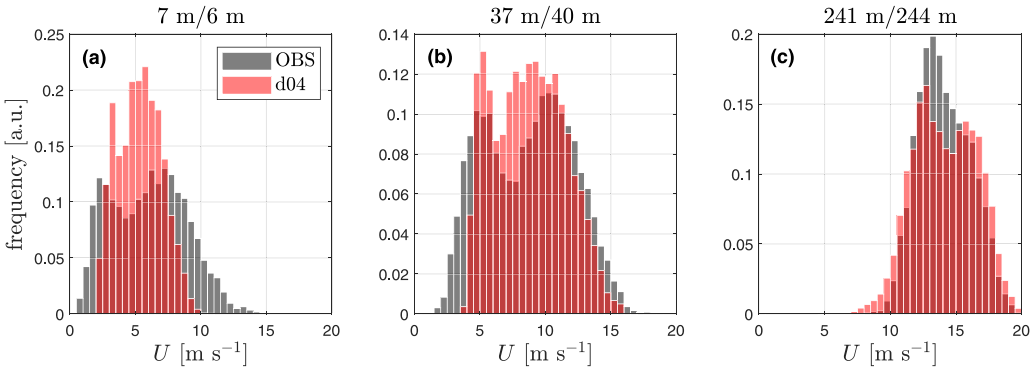

Fig. 5. Wind speed histograms of the horizontal velocity from 12-s resampled sonic anemometer observations and 12-s LES domain d04 output at three heights: 7, 37, and 241 m in panels (a), (b), and (c), respectively, at Østerild. a.u. refers to arbitrary units.

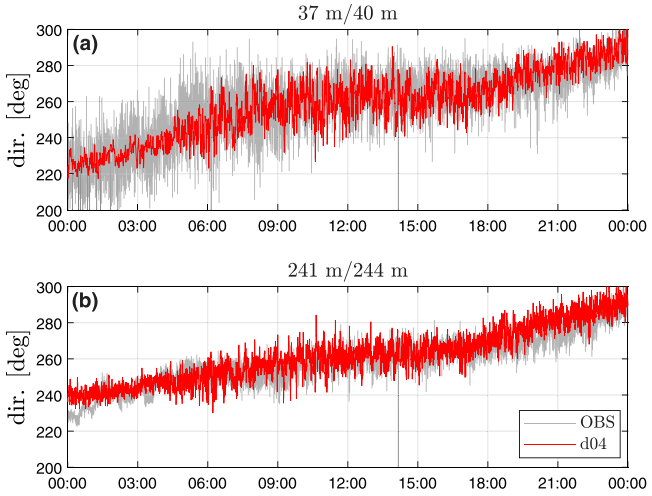

Fig. 6. Similar to Fig. 4 but for the wind direction at two different observational heights: 37 and 241 m in panels (a) and (b), respectively. For the simulated winds, the closest vertical levels to the observations are at ≈40, and 244 m.

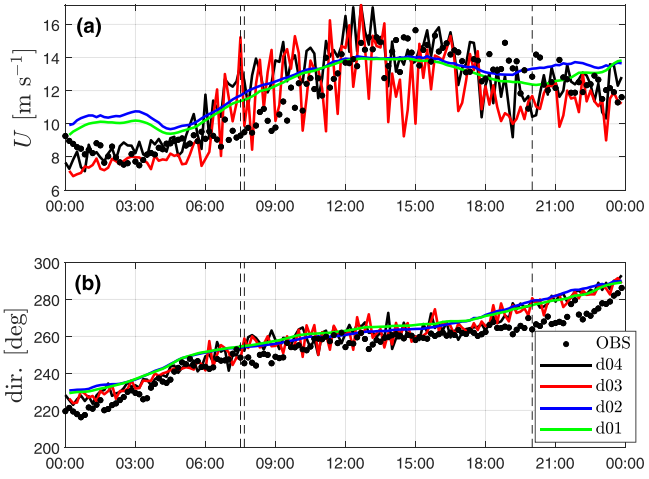

Fig. 7. Time series of (a) horizontal velocity at ≈110 m and (b) wind direction at ≈40 m from 10-min means of cup anemometer and wind vane observations (OBS in markers) at Østerild. 10-min instantaneous output from the three outermost domains (d01–d03) and 10-min means from the innermost LES domain (d04) are shown in different lines. Vertical dashed lines correspond to periods in which vertical profiles are further analyzed.

mesoscale winds do not capture the observed variability in the 10-min cup anemometer means. However, the variability of the 10-min mean winds of the two LES domains seems to be larger than that of the observations, particularly from 06:00 onwards. Within the period 00:00–03:00, the variance of the 10-min mean wind measured by the cup anemometer at 106 m is 0.26 m^2 s^{-2}, whereas that of the 10-min instantaneous winds from d03 and 10-min mean winds from d04 is 0.15 and 0.27 m^2 s^{-2}, respectively, at ≈113 m. Within the period 12:00–15:00, the equivalent variances are 0.69, 5.15, and 1.85 m^2 s^{-2} for the observations, d03, and d04, respectively; the d03 value is clearly dominated by the decreasing trend within that 3-h period but a detrended 3-h time series also shows a high variance (3.39 m^2 s^{-2}).

For the wind direction, we can see all domains' output closely following the observations from the vane at 40 m (Fig. 7b). The variability in the observed direction (standard deviation of 5.13°) is interestingly close to that of the output of the LES domains, 5.23° and 5.11°, for d04 and d03, respectively. Note that the 10-min direction values of d04 are computed from the 10-min mean zonal and meridional winds.

The selected day also presents some other interesting features. As illustrated in Fig. 8b, during the early morning hours (00:00–06:00), the heat flux measured by the sonic anemometer at 37 m is less than −0.03 K m s^{-1}, increasing up to 0.31 K m s^{-1} at 12:00 and slowly reaching values below zero from 19:00 onwards, which shows the wide range of atmospheric stability conditions. At the closest to observed vertical level (≈40 m), the total simulated sensible heat flux (resolved plus SGS part) from the d04 output agrees well with that of the sonic observations: the mean value within 00:00–03:00 is −0.041 K m s^{-1}. However, the heat flux at this level starts to increase in the simulations much earlier than in the observations, turning positive already at 04:30. It becomes negative and follows well the observed values from 19:00 onwards. Also, during the first five hours, both simulations and observations of the along-wind variance at ≈40 m are quite close and low (see Fig. 8a). In general, the simulated along-wind variance at the three vertical levels agrees well with the observations throughout the day, with the measurements at 103-m showing the lowest values from the three analyzed levels particularly within the convective part of the day; the simulated variances at 110 m are not systematically the lowest within this period.

In Fig. 7a, the horizontal velocity output of the LES domains d03 and d04 at 110 m, particularly that of d03, largely fluctuates around the mesoscale values within the period 06:00–15:00. Within the same period, the simulated sensible heat flux is much larger than the observed heat flux from the sonic anemometers at three heights (Fig. 8b). To study these differences more in detail, we extract output from observations and simulations at 07:30 and Fig. 9 shows vertical profiles of the horizontal wind speed, wind direction and along-wind variance from both the sonic and cup anemometers, and the output of the simulations at Østerild from the different domains.

As illustrated, at this particular time, the wind speeds are strongly overestimated (by more than 5 m s^{-1} at some vertical levels) by the

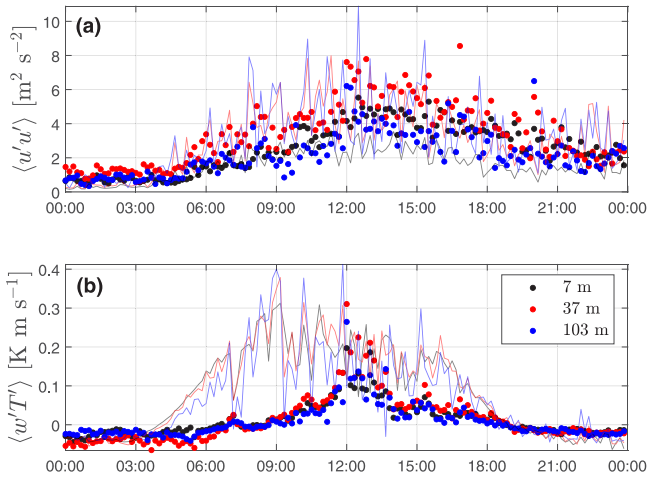

Fig. 8. 10-min time series of (a) along-wind variance and (b) sensible heat flux at three vertical levels from sonic-anemometer observations and output for domain d04.

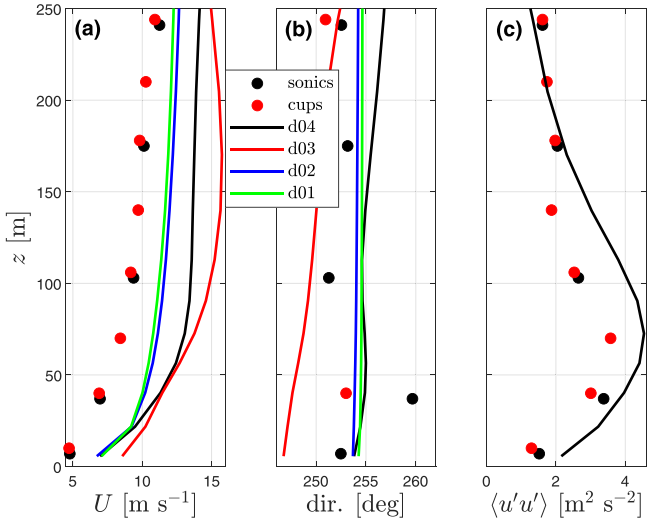

Fig. 9. Vertical profiles of (a) horizontal velocity, (b) wind direction, and (c) along-wind variance at 07:30 at Østerild. 10-min means of cup and sonic anemometer observations are shown in markers. The lines show instantaneous output for domains d01–d03 and 10-min means (or 10-min total variance) from output of domain 04.

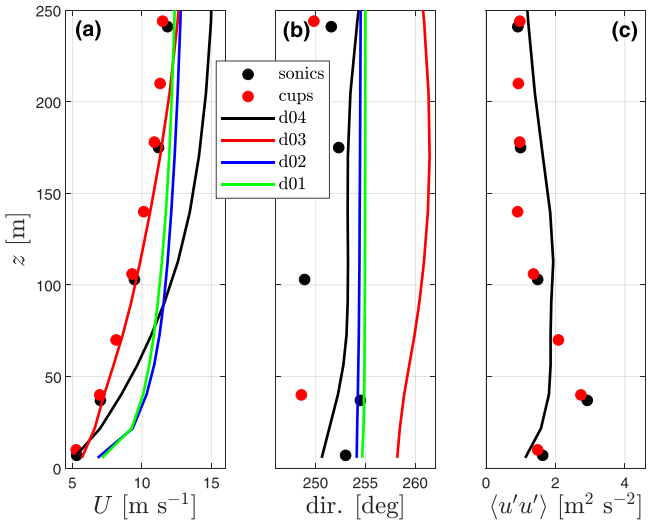

Fig. 10. Similar to Fig. 9 but vertical profiles correspond to 07:40.

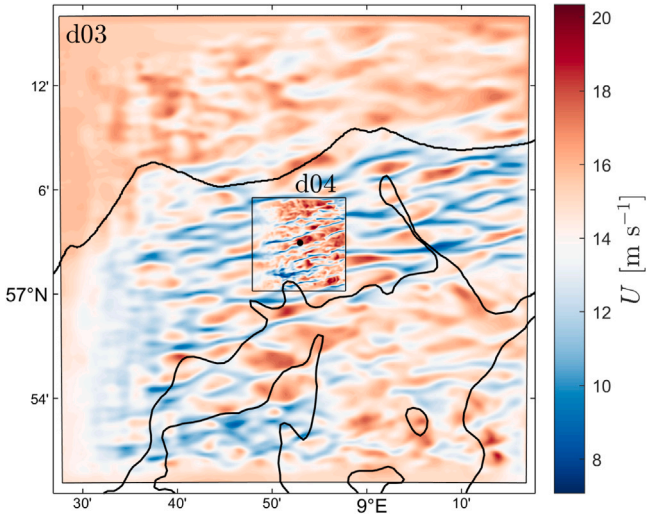

Fig. 11. Instantaneous horizontal velocity magnitude from the two innermost LES domains at 12:00 at ≈110 m. Domains' boundaries are in thin black lines and the position of the Østerild meteorological mast in the black circle.

simulations, in particular those from the LES domains (d03 and d04). The wind direction is well predicted by all domains' output, with that from the LES d03 domain showing the largest discrepancy from the other domains. Interestingly, when compared to the observations, the along-wind variance is well predicted by the output of the innermost LES domain (d04) both in its value and the behavior of the vertical profile: both observations and simulations show increasing values up to about 70 m, both decreasing slowly upwards. One explanation for the discrepancy of the vertical wind profiles from d03 is the presence of under-resolved convective roll structures that occur during the selected analysis period as a result of its relatively coarse resolution relative to the forcing. These structures can also explain the slightly greater than observed variance within d04, resulting from their advection into and subsequent interactions with the perturbations and evolving turbulence features within d04. At 07:30, Østerild 'samples' these structures developed at d03 under an area with very high wind speed, whereas just 10 min later (see Fig. 10), the Østerild position is under an area in which the structure has a much lower wind speed (nearly 6 m s^{-1} lower). These structures do not appear in the observations of this particular day and are responsible for the large variability of the 10-min means of the innermost LES domains during a large portion of the convective period of the day. They are also visible in the 12-s output of the innermost LES domains in Fig. 4, although less evident due to the frequency of the time series. In Fig. 11, we illustrate the instantaneous output at 12:00 and at the height of ≈110 m of the horizontal velocity magnitude of the two innermost LES domains in which these structures are clearly portrayed (this output is the only available covering fully the domains within the convective period). The horizontal velocity magnitude varies more than 12 m s^{-1} within the domains.

We also select another time (20:00), but at this hour both observed and simulated sensible heat fluxes are closer than in the previous cases. At ≈40 m, the simulated sensible heat flux is −0.016 K m s^{-1}, whereas the observed value is −0.009 K m s^{-1}. As illustrated in Fig. 12, at this time the vertical profiles of simulated and observed wind speed are in good agreement, both showing a linear increase with height, which is a typical behavior of a close to stable atmosphere. Simulated directions are systematically biased ≈10° from the observations. In this case, the along-wind variance is well predicted by the LES d04: both observations and simulations show nearly the same value at each vertical level.

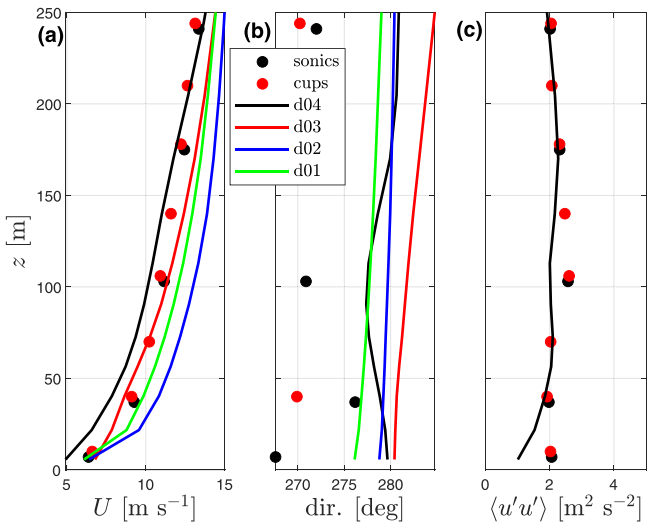

Fig. 12. Similar to Fig. 9 but for the time 20:00 at Østerild.

4.2. Full year intercomparison

For the analysis of the full year of 2017, we filter out all 10-min periods in which, first, the mean wind speed measured by any of the cup anemometers is below 1 m s^{-1}, which helps removing periods, e.g., when the instruments freeze, second, the wind direction measured by any of the wind vanes is within $0 \pm 15°$, which decreases the influence of the wakes of the wind turbines north of the mast, and third, 10-min periods where the 1-Hz records of the cup anemometers are not entirely available. Without such filtering, the dataset consists of 51987 out of 52560 possible 10-min periods within the entire 2017 and after filtering, 45868 10-min periods remain for the analysis. Since the simulation output covers the entire full year, the intercomparison is performed only during the periods in which observations are available after filtering.

Fig. 13 shows observed and simulated wind roses at 244 m, the height at which the uppermost cup anemometer and wind vane are mounted. As illustrated, westerlies are predominant at Østerild and the simulations from the innermost LES domain (d04) capture well both the direction and the ranges of wind speed within most of the directions. From the observed wind rose, a 'notch' appears at the north direction due to 'wake' filtering but these are the least predominant directions at this site.

The good agreement between the wind climatology based on the observations and the simulations at Østerild is partly due to a good match between the roughness length used in our WRF model configuration and that of the observations. The roughness length used in the model is read from the vegetation parameter table associated with the MODIS land cover classification with minimum and maximum values of 0.20 and 0.50 m, respectively, and is updated daily at the grid point of Østerild. There are different approaches to estimate the surface roughness length z_0 from observations: here we assume that the logarithmic wind profile is valid within the first tens of meters of the neutral atmosphere, which results in

$$z_0 = z \exp\left(\kappa U / u_*\right)^{-1}, \tag{8}$$

where z is the height of observation, u_* the friction velocity, and $\kappa = 0.4$ the von Kármán constant. By using Eq. (8) and observations from a single vertical level only, we reduce the uncertainty on the z_0 estimations. Therefore, and only for deriving z_0 values from observations for the full year, we use 10-min statistics based on the sonic anemometer at 37 m. Due to the availability of the instrument during 2017, we have only 17852 10-min periods. Since Eq. (8) is only valid for neutral atmospheric conditions, we select 10-min periods within the range $|z/L| \leq 0.05$ m^{-1}, where L is the Obukhov length, which is computed from the sonic anemometer means and fluxes as

$$L = -\frac{\langle T_s \rangle u_*^3}{\kappa g \langle w' T_s' \rangle}, \tag{9}$$

where T_s is the sonic anemometer temperature, g the Earth's gravitational acceleration, and $\langle w' T_s' \rangle$ the sonic's kinematic heat flux, which has similar values to the virtual potential kinematic heat flux. We also apply the corrections suggested by Liu et al. [35] for the computation of the heat flux from this particular sonic anemometer. Further, from a direction analysis of z_0 estimates under neutral conditions, Peña [18] showed that for the predominant westerlies at Østerild, z_0 derived from Eq. (8) is the lowest: this is expected as forest surrounds the mast position except west of the mast where there is a clearing (see Fig. 1). Therefore, we also restrict the roughness analysis to winds from the direction $270 \pm 15°$ based on the sonic-derived wind direction. A total of 1428 10-min periods then remain after the directional and atmospheric stability criteria are applied to the observations. Fig. 14(a) shows a comparison between the roughness length seen at Østerild by the innermost LES domain (d04) and that derived from the sonic anemometer observations. The 10-min estimates from the observations are averaged monthly and yearly as $\exp\left(\langle \log z_0 \rangle\right)$. The yearly observed value is 0.2617 m (black dashed line), which is close to both the omnidirectional yearly average from the values at d04 (0.3314 m in the red dashed line) and the value (0.2492 m), which was derived from a similar analysis using the sonic anemometer at 37 m during a 4-year period under the same direction range $270 \pm 15°$ [18]. As illustrated, z_0 at d04 depicts a clear seasonal change peaking during the summer months because, according to the land cover used in the WRF model (Fig. 2b), Østerild is a mixed forest. The derived monthly averages from the observations are close to those at d04 with regards to their impact on the wind; a relative change of 20% in roughness length value results in a relative change of 2% in mean wind assuming the geostrophic drag law and same forcing. However, they do not show the seasonal trend partly because we concentrate the analysis within the directions of the forest clearing; the value in July is indeed the lowest.

Fig. 14(b) shows the year-long time series of 10-min mean winds from both observations from the cup anemometer at 106 m and output from the LES d04 domain at ≈110 m. As illustrated, the simulations follow well the observations, which portray the wide range of wind speeds at the site. To understand how accurate the simulated time series of wind speed are, we compare the histograms of wind speed based on the observations and simulations for the vertical level at ≈110 m. Fig. 15(a) illustrates the year-long histograms of wind speed from the output of the LES domain d04 at ≈110 m and the cup anemometer at 106 m.

As illustrated, for this particular height the histograms agree closely, with the simulations generally showing higher frequencies of occurrence for winds $\gtrapprox 8$ m s^{-1}. For visualization purposes we do not include the histogram based on the output of the mesoscale domain d02, which has a similar behavior as that of domain d04 but it is slightly biased towards higher wind speeds with relative lower frequencies at the histogram's peak. However, we show the Weibull distributions of observed and simulated mean wind speeds. These are computed from the Weibull shape and scale parameters derived via a maximum likelihood estimator that uses the time series of wind speed. Fig. 15(a) shows that these all-sectors Weibull distributions fit the wind speed histograms well but underestimate the frequency of the histogram peak. Also, and most importantly for wind energy purposes, both observed and d04-simulated Weibull distributions are close to each other, which shows, first, a very good agreement between the observed and simulated Weibull parameters, and second, that the simulated and observed power density, which is a measure of the energy available in the wind, are very close. The power density is defined as

$$P_d = \frac{1}{2}\frac{1}{N}\rho \sum_{i=1}^{N} U_i^3, \tag{10}$$

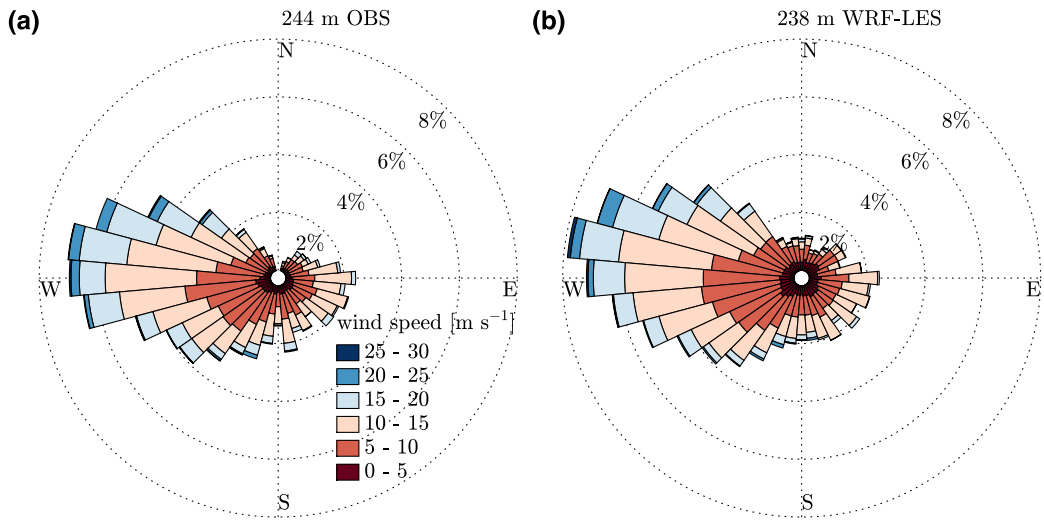

Fig. 13. Wind roses based on (a) observations from the cup anemometer and vane at 244 m and (b) output from the simulations at ≈238 m from the innermost LES domain (d04) at Østerild during 2017.

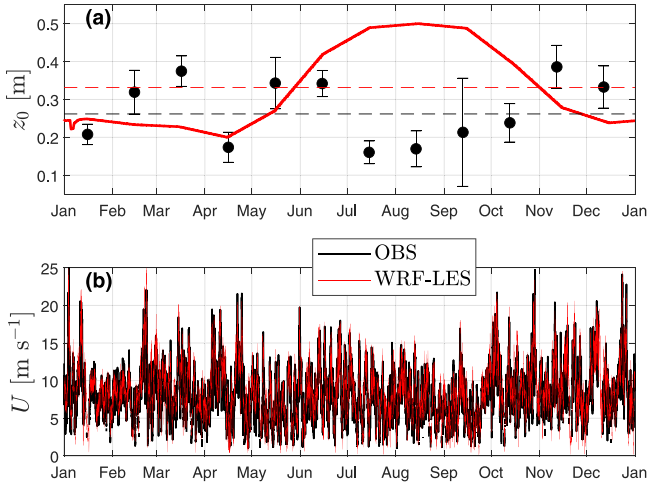

Fig. 14. (a) Roughness length z_0 estimated from sonic anemometer observations and that used by the innermost LES domain d04 for 2017 at Østerild (see text for details). The circles represent the value $\exp(\langle \log z_0 \rangle)$ within 30-day periods and the error bar ±one standard error. The dashed lines show the value $\exp(\langle \log z_0 \rangle)$ for 1428 10-min z_0 estimates from the observations (in black) and the mean of the values used by the simulations (in red). (b) Time series of the 10-min mean wind speed from the cup anemometer at 106 m and the LES d04 simulations at 110 m.

where we assume a constant air density $\rho = 1.225$ kg m^{-3}, and N is the amount of samples. This is further illustrated in Fig. 15(b): power densities computed from time series of the observations and the output of the LES domain d04 are close at each vertical level, and those computed from the output of the mesoscale domain d02, although also close, are the ones generally deviating the most.

In Fig. 16, we also show year-long histograms of a turbulence parameter, the standard deviation of the wind speed. The figure illustrates the results for computations based on the analysis of the 10-min statistics of the 1-Hz cup anemometer observations at 106 m, similarly on the analysis of 10-min statistics of the 12-s output of the LES domain d04, and on estimations based on the 1-h instantaneous output of the mesoscale domain d02. Here, to estimate σ_U from the output of d02 we assume that

$$\sigma_U \approx \left(\frac{2}{3}e\right)^{1/2}. \tag{11}$$

The histograms in Fig. 16 reflect the wide range of atmospheric turbulence conditions at the site. The histogram based on the output of the LES domain d04 (in red) shows a very close resemblance to that from the observations (in gray). The largest discrepancies between the latter two histograms appear within the values close to zero (in the first bin), where the frequency of simulated values is close to five times that of the observations. This is partly due to the wind speed filter applied on the cup anemometer records, which also results in the filtering of a portion of very low observed turbulent conditions. It is also partly due to deficiencies in resolving turbulence, particularly during nighttime (as we show in more detail in Section 4.3), where stable atmospheric conditions dominate at Østerild and turbulence is low. Based on analysis of velocity spectra from the sonic anemometers at Østerild, Peña [18] showed that under stable conditions, the atmospheric flow has the lowest turbulence length scales within the whole extension of the mast; these cannot be resolved by the innermost LES domain d04, whose effective resolution is $\approx 6\Delta x = 300$ m. Within the high turbulence range ($\sigma_U \geq 2$ m s^{-1}), the d04-based turbulence values are also more frequent than those of the observations; the latter showing higher frequencies within the range ($0.7 \leq \sigma_U \leq 1.8$) m s^{-1}. The largest differences, when comparing simulation-based values to the observations, clearly appear for the mesoscale-derived turbulence measures from d02. Turbulence levels from d02 concentrate within a narrower portion and closer to the lower side of the histogram ($0 \leq \sigma_U \leq 2$) m s^{-1}. The mesoscale-based histogram is bimodal: the peak at wind standard deviation values close to zero combines low wind and low turbulence periods mainly occurring during the late night and early morning. For the rest of the vertical levels (not shown), the bimodal behavior of the mesoscale-derived output is less clear closer to the surface and is enhanced the higher the level examined. When comparing the observed histograms with the LES d04-based output (also not shown) and with respect to the results at ≈110 m in Fig. 16, the simulations are slightly biased towards lower values of wind speed standard deviation closer to the surface, whereas they are slightly biased towards higher values of wind speed standard deviation upwards.

With regards to TI, which combines both the abilities of the model and its configuration to capture both turbulence and mean winds, we analyze its behavior as function of wind speed in Fig. 17 for four of the matching (observations/simulations) vertical levels. There, the full-year 10-min TI values computed for both simulations and observations are binned within wind speed bins to ease the comparison.

As illustrated, for all vertical levels both simulations and observations show a wide range of TI values (0%–30%), particularly at low wind speeds, which reflect both the wide variety of turbulence and

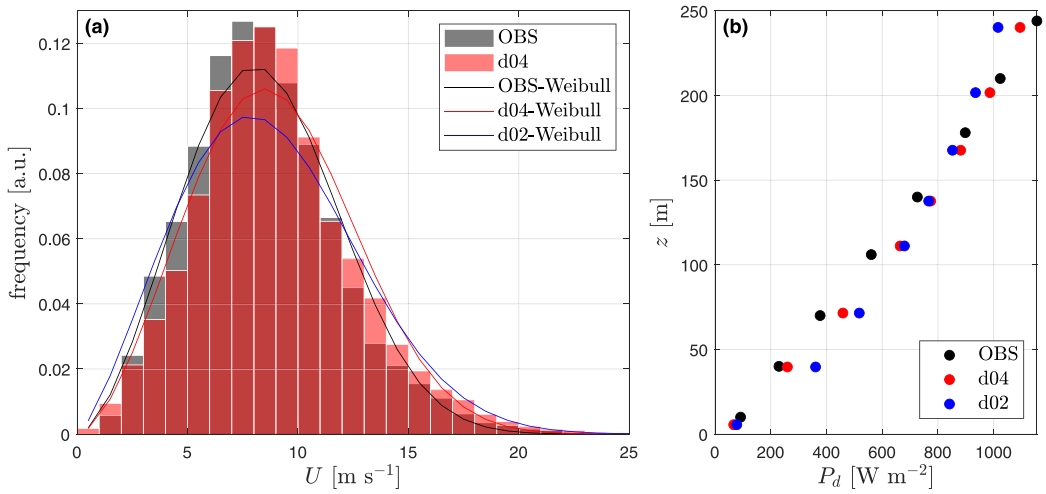

Fig. 15. (a) Wind speed histograms based on the 10-min means of the 106-m cup anemometer and 10-min means of the ≈110-m output of the LES domain d04. The solid lines are based on maximum likelihood estimates of the parameters of the Weibull distribution using the time series of wind speeds, where we also show the distribution computed from 1-h instantaneous values of the ≈110-m output of the mesoscale domain d02. (b) Vertical profile of the power density computed from the different time series of wind speed (see text for details).

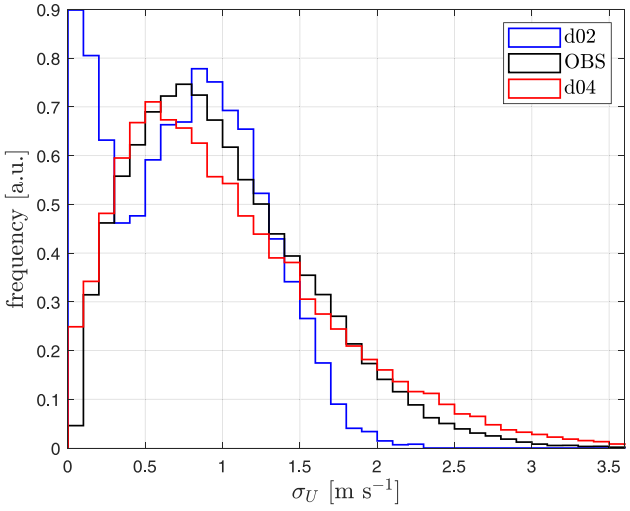

Fig. 16. Wind speed standard deviation stairs-like histogram based on 1-year output of the LES domain d04 and mesoscale domain d02 at ≈110 m, and the observations from the cup anemometer at 106 m. The cup- and d04-based results are from the analysis of the 10-min statistics, and the d02-based results from instantaneous 1-h model output.

atmospheric stability conditions at Østerild. Although not that clear at the lowest displayed height (Fig. 17a), the simulated and observed TI behaves similarly as function of wind speed. At high wind speeds, TI tends to stabilize, which is the typical behavior of TI over flat terrain under near-neutral atmospheric stability conditions [36]. When approaching the low wind speed ranges, we observe the effect of atmospheric stability on the TI both on the mean within each wind speed bin and on the spread of the values (shown in the error bars). In general, the observed mean turbulence levels are fairly matched by those computed from the simulations. The simulations show lower TIs for $U \lessapprox 7$ m s^{-1}, which is partly due to lack of turbulence in the simulations under some late evening and early morning periods mostly, where wind speeds are low, but also because the simulated wind speeds are higher than the observations during these periods. For $U \gtrapprox 7$ m s^{-1}, the simulations tend to show higher TIs, a behavior intensified the higher the vertical level. This is mainly due to an increased bias towards higher turbulence on the simulations compared to the observations as explained when presenting the turbulence histogram in Fig. 16. Fig. 17(a), in particular, shows the limitations of the modeling system in its current configuration, as at this level the model has difficulties to resolve turbulence (or cannot at all), particularly under the low wind conditions, where stable atmospheric conditions, characterized by relatively small turbulent eddies, could be dominant. The year-long average of simulated sensible heat flux is −0.032 and 0.089 K m s^{-1} within the nighttime (from 21:00–03:00) and daytime (from 09:00–15:00), respectively, at 40 m, thus, these periods largely portray stable and unstable stability conditions, respectively. Under the same daytime and nighttime periods, the year-long average of simulated along-wind variance is 1.83 and 0.97 m s^{-2}, respectively.

We explore the behavior of the simulated and observed velocity spectrum for the full year in Fig. 18. Both the time series of 10-min mean wind speeds from the cup anemometer at 106 m and the output of the LES domain d04 at ≈110 m are split into 73 time series that are 5-day long. The spectra computed from these 73 time series are ensemble averaged and the average spectrum is that illustrated in the figure. Similarly, we compute an average spectrum from the 1-h time series of instantaneous winds that are output from the mesoscale domain d02 at ≈110 m.

As illustrated, the observations show the expected behavior within the mesoscale range, i.e., the spectrum follows the $-5/3$ slope (also shown). The simulated spectrum from the mesoscale domain d02 and the innermost LES domain d04 follows rather well the observed spectrum down to frequencies close to 2 h and 1 h, respectively. There are no signs of decay of any of the simulated spectra at the high resolved frequencies when compared to the observed spectrum, which is a typical feature of mesoscale flow models [37]. Conversely, the simulated spectrum from the LES domain d04 shows higher energy content than the observed spectrum from frequencies close to 1 h up to 20 min. This is most probably due to artifacts of the simulations: first, by perturbing the two innermost LES domains, we could artificially increase the variability of the 10-min mean winds, and second, spurious convective roll structures occasionally forming on d03 could increase the variability on d04 as those rolls advect into it and interact with the perturbations and developing turbulence therein.

4.3. Sensitivity to LES inflow perturbations

The high energy content within the high frequencies of the simulated winds from the output of the LES domain d04 when perturbing both LES domains d03/d04, in particular, show us the need to explore the sensitivity on the output of this particular domain to different

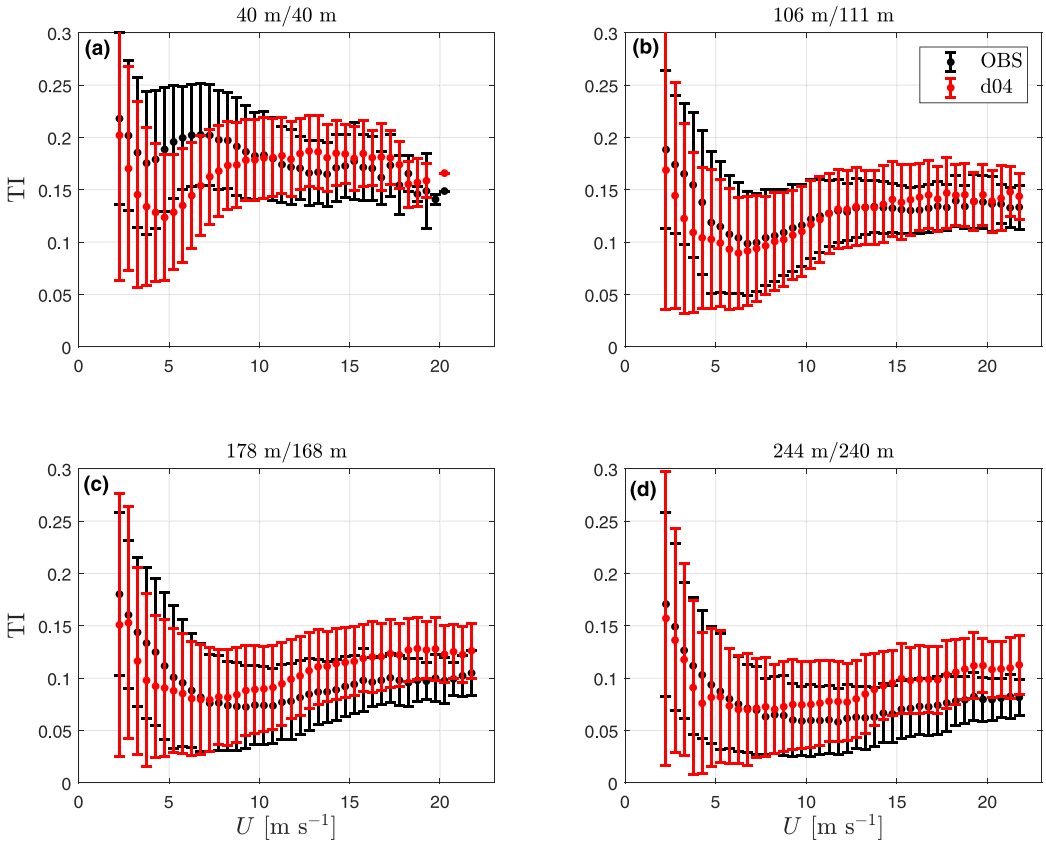

Fig. 17. Turbulence intensity (TI) as function of the wind speed at (a) 40 m, (b) 106 m, (c) 178 m, and (d) 244 m based on the 10-min statistics computed using the output of the innermost LES domain d04 and the cup anemometer observations. The TI values are binned within 0.5 m s^{-1} intervals; the mean for each bin is shown in filled circles and the error bars show ±1 standard deviation within the bin. Each frame title shows the observational height and simulated mean vertical level.

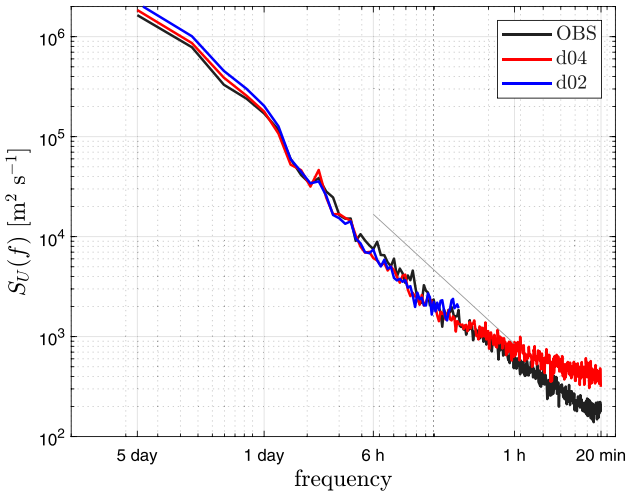

Fig. 18. Wind speed averaged power spectrum based on the 10-min time series of the output of the LES domain d04 and 1-h time series output of the mesoscale domain d02 at 110 m, and the 10-min time series of the cup anemometer observations at 106 m. The mean spectrum is derived from 5-day long time series for the entire 2017. The spectral slope of −5/3 is shown in the gray line.

alternatives for inflow perturbation. Therefore, we also perform two more sets of simulations: one with inflow perturbation at the d04 boundaries only (d04 in Fig. 19) and the other perturbing the d03 boundaries only (d03 in Fig. 19). Since, we cannot afford three sets of simulations for an entire year, we choose a 10-day period, where we observe a variety of wind and turbulence conditions, high and low wind and turbulence events, and clear diurnal cycles. Fig. 19 illustrates the time series of three 10-min statistics, namely the mean wind speed, along-wind variance, and turbulence intensity, within the selected 10-day period from both the output of the innermost LES domain d04 from the three sets of simulations at ≈ 110 m and the cup anemometer observations at 106 m.

As illustrated in Fig. 19(a), all three simulations capture well the observed mean wind speed during the 10-day period. During the few events where observations deviate noticeably from the observations (e.g., the late afternoon on June 15), all three of the simulations deviate similarly. Differences become clearer when looking at the along-wind variance time series in Fig. 19(b). All three simulations capture the trends of the observed variance. However, the d03 simulation frequently underpredicts the variance relative to the observations, particularly during the late evening and early morning periods during which the observed levels of turbulence are high. This is also clearly reflected in the TI time series shown in Fig. 19(c). One can also notice in the along-wind variance time series that about midnight during several of the diurnal cycles, all of the simulations underpredict the observed variance during low turbulence periods, e.g., between June 10/June 11 and June 17/June 18. This mismatch is sometimes hidden in the TI time series as the wind speed can be higher from the simulations compared to the observations, e.g., during the early morning of June 11. Further, one can also notice the higher variability of the along-wind variance from the simulation d03/d04 compared to simulation d04, particularly at high turbulence levels. Table 2 provides the root mean square error (RMSE) between the 10-min time series of observations and the output of the three simulations. As shown, the largest RMSEs for the mean wind speed, along-wind variance and TI are computed using the d03 simulation. For the along-wind variance, the d04 simulation has the lowest RMSE, whereas the simulation d03/d04 has the lowest RMSE for

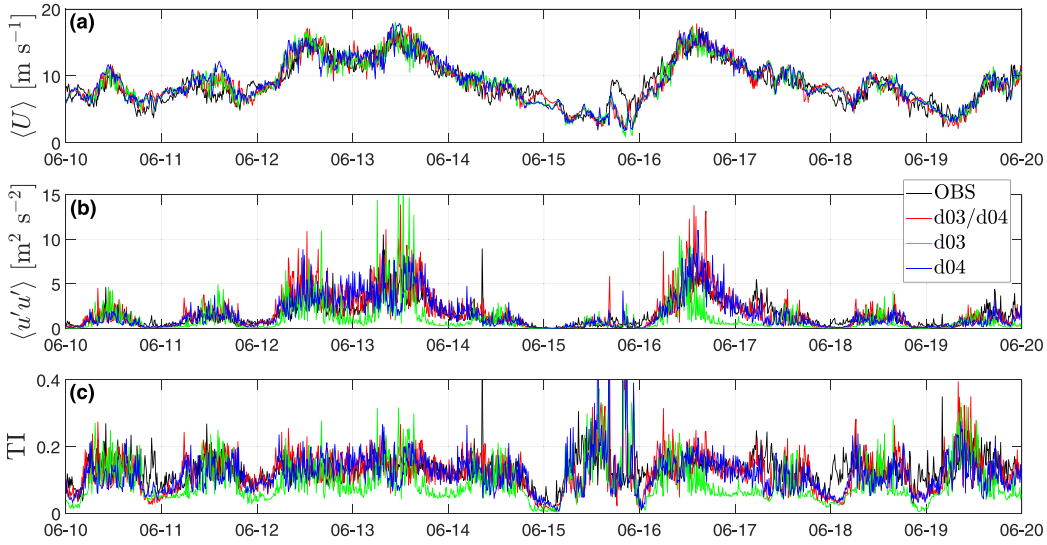

Fig. 19. 10-day long time series of 10-min statistics from the cup anemometer observations at 106 m and output of the LES domain d04 at 110 m for three different inflow perturbation configurations (see text for details). Panels illustrate (a) mean wind speed, (b) along-wind variance, and (c) turbulence intensity (TI).

Table 2
Root mean square error (RMSE) of three flow characteristics between the simulated and observed 10-min time series at ≈110 m for the three simulations within the inflow perturbation sensitivity study.

Variable/simulation	d03/d04	d03	d04
$\langle U \rangle$ [m s^{-1}]	**1.540**	1.573	1.647
$\langle u'u' \rangle$ [m^2 s^{-2}]	1.443	1.639	**1.263**
TI	**0.061**	0.077	0.068

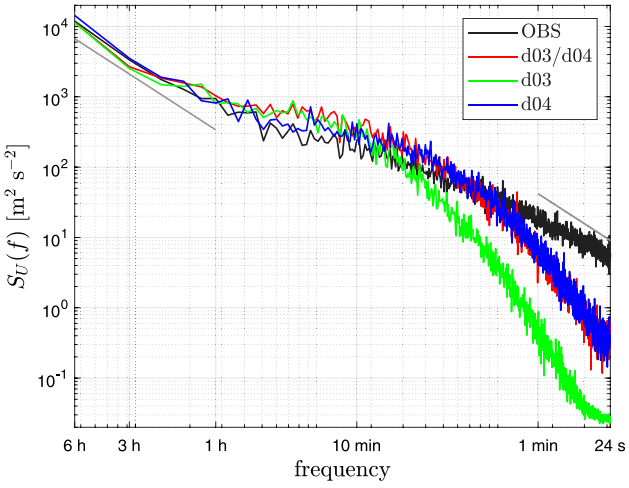

Fig. 20. Wind speed averaged power spectrum based on the 12-s time series of the output of the LES domain d04 at 111 m from three configurations of the inflow perturbations, and the 10-Hz time series of the cup anemometer observations at 106 m. The mean spectrum is derived from 6-h long time series for a 10-day period. The spectral slope of $-5/3$ is shown in the gray line.

the mean wind speed. For this particular 10-day period, if we want to reproduce the best TI estimates, perturbing both LES domains provide the lowest error.

For completeness, we illustrate the velocity spectra within the 10-day period computed from both the observations and the three different simulations at ≈110 m in Fig. 20. Since we restrict the analysis to a single 10-day period, we are able to use the time series of 12-s simulated and 10-Hz observed wind speeds. The spectrum of the d04 simulation, where the perturbations are applied on the boundaries of the innermost LES domain d04 only, follows the observed spectrum the closest within the range of frequencies 6 h to 10 min, with no clear signs of higher wind variability within the range of frequencies between 10 min and 1 h. The d03 and d03/d04 simulations follow closely each other up to a frequency close to 10 min and both portray higher variability than the observations within the range of frequencies between 10 min and 1 h, as similarly illustrated for the year-long analysis in Fig. 18. From a frequency close to 10 min to the highest frequencies, the variability of the d03 simulation drops the fastest, whereas both the d03/d04 and d04 simulations exhibit similar behavior, only dropping relative to the observations at frequencies corresponding to a few minutes or less.

5. Discussion

This study demonstrates a capability to use a multiscale modeling system to reproduce both the mean wind and the turbulence conditions (which are part of the so-called site conditions) at a particular site with high fidelity. More evaluations of the modeling system, and of its setup and configuration, under different topographical and climatological conditions are envisioned for the future to fully understand the capability of the system. This will be highly beneficial for the exploitation of wind energy and for the understanding of the atmospheric turbulence conditions also where measurements are not available. It should be noted that the ability to reproduce flow characteristics of this modeling system depends strongly on the topographical inputs. For Østerild, the roughness length value used in the simulations matches well the value estimated from the observations but this might not be the case for many other sites. The roughness length values are here converted from the MODIS land cover dataset, which is not as detailed as others [38] but has global coverage and is therefore attractive for building robust modeling systems that can be utilized anywhere. Due to the orography conditions at Østerild, the choice of a coarse terrain elevation dataset does not play an important role on the simulation output; however, usage of high-resolution datasets is necessary when simulating atmospheric flow over complex terrain [39]. Also, we do not study the sensitivity of simulations to spinup times and use the minimum recommended value for the WRF model. We are aware that, e.g., a mismatch between the topographical inputs used for the simulations in the WRF model and those from the reanalysis can lead to the need of increased spinup times.

It is important to point out that we do not claim that our numerical setup and model configuration are the most suitable to perform these

types of simulations using the WRF model. Neither that this is the most efficient configuration for optimized computational costs. The main objective of these simulations is to demonstrate that this type of year-long (or longer) simulations, where we resolve the large turbulent scales, are affordable using a WRF-LES-based system. Further, we demonstrate that one can obtain both mean and turbulent-related parameters, which are more comparable and in better agreement with measurements than similar parameters derived from mesoscale domain output, which is typically the product used when performing year-long simulations.

The ability of the innermost LES domains to resolve turbulence with the chosen horizontal spatial grid spacing is limited, especially under stable atmospheric conditions at this particular site. Based on analysis of the Østerild sonic anemometer observations and the 3D turbulence spectral model of Mann [40], the turbulence length scales were found to be generally smaller than 50 m within the first 150 m from the ground and within a broad range of stable atmospheric conditions [18]. With our simulation setup, we are obviously missing a large portion of the turbulence spectrum under these conditions. In Peña [18], the measure of turbulence anisotropy above 100 m under stable atmospheric conditions was doubled by the value found under unstable conditions and for future work we aim at studying whether WRF-LES-based simulations, at a much higher spatial resolution than the present study, are capable of reproducing these turbulence characteristics, which might have an impact on wind turbine's response.

When configuring this type of multiscale simulations, we want to resolve the eddies with the most energy content under all atmospheric conditions, which translated into trying the highest spatial resolution possible. In parallel, we could also try to avoid the so-called gray zone regime in which the horizontal grid spacing is of the same order of the PBL height, where resolve convective motions might become unrealistic [41]. For the case of northern Denmark this means $\Delta x \approx$ 100–1000 m. With $\Delta x \lessapprox 250$ m and with nest grid ratios of 1:3 or 1:5, typically used in real forcing simulations with the WRF model, we cannot avoid the gray zone. Under a number of conditions, our setup is obviously not optimal (convective structures are being simulated in the LES domain d03 but not observed in Fig. 11) and future work points at analyzing the impact of larger grid ratios and/or usage of new PBL schemes accounting for 3D turbulence effects within the gray zone [42].

Further, as illustrated in Section 4.3 for a 10-day period, the perturbations we impose in domain d03 might artificially impact the turbulence spectrum, which increases the simulated along-wind variance. This could be partly the reason of the good match of TI levels between simulations and observations in Fig. 17 and the overprediction of simulated TI at high wind speeds. In addition, the sizes of the LES domains we choose might limit, under a number of conditions, the development of turbulence before the flow reaches the Østerild meteorological mast. The mast is 5 km from the closest domain d04 boundary; for a flow case portraying a convective atmosphere, Muñoz-Esparza and Kosović [33] showed that TKE, and momentum and heat fluxes needed about 30 km to develop, whereas use of CPM could reduce this to half the value, which is bigger than the size of our innermost LES domain. Examination of multiscale simulations that apply larger domain sizes and CPMs adapted to non-neutral atmospheres [33] is also part of our future plans.

6. Conclusions

A full-year multiscale atmospheric simulation combining both mesoscale weather and explicit turbulence simulation is performed at a largely flat and rough site in northern Denmark. Results from an LES domain nested within a mesoscale simulation, all within the WRF model, are assessed by comparing both mean winds and turbulence measures with observations recorded with a heavily instrumented 250-m high-quality meteorological mast.

Post-processed 10-min mean wind speeds and directions from the output of the simulation's innermost LES domain show very good agreement with cup anemometer and wind vane observations for the entire year and for the extension of the mast. The wind climatology, both in terms of wind roses and histograms of mean winds, is well represented by the simulation; further the observed power density at the different vertical levels is better predicted by the innermost LES domain output than by the mesoscale domain output with the finest resolution.

Histograms of post-processed 10-min along-wind variances from the output of the simulation's innermost LES domain agree very well with those from the observations. However, the instantaneous hourly output of the high-resolution mesoscale domain has difficulties capturing the high levels of variance, frequently producing very low variances when compared to the observations. The behavior of observed turbulence intensity with wind speed is very well captured by the innermost LES domain output at most vertical levels, with the best agreements at the greatest heights, and deteriorating with increasing proximity to the surface. Turbulence intensity also tends to be underestimated and overestimated by the simulations under low and high wind speed ranges, respectively.

Spectral analysis shows that the innermost LES domain output presents larger variability than the observations at high frequencies. A sensitivity study reveals that the increased variability is partly due to application of the CPM to both LES domains, rather than just the innermost one. For this particular 10-day period, the observed variability can be better matched by perturbing the innermost LES domain only.

CRediT authorship contribution statement

Alfredo Peña: Writing – review & editing, Writing – original draft, Visualization, Validation, Software, Resources, Methodology, Investigation, Funding acquisition, Formal analysis, Data curation, Conceptualization. **Jeffrey D. Mirocha:** Writing – review & editing, Software, Methodology, Conceptualization.

Declaration of competing interest

The authors declare the following financial interests/personal relationships which may be considered as potential competing interests: Alfredo Pena reports financial support was provided by Independent Research Fund Denmark. Alfredo Pena reports financial support was provided by Ministry of Foreign Affairs of Denmark. Jeffrey D. Mirocha reports financial support was provided by US Department of Energy.

Data and code availability

The WRF model with the corresponding implementations can be found at https://github.com/a2e-mmc/WRF. The post-processed simulated data for d04 at the Østerild mast position, as well as that of d02, which are used to produced the figures are available at https://figshare.com/s/894bdb0cceb24c294b3c [43]. There, examples of the WRF model input files, `namelist.input` and a `namelist.wps`, which are used for one of the 37 10-day-long runs are also available. The meteorological mast data are proprietary data from DTU and only portions of them are available upon request.

Acknowledgments

The work is partly funded by Independent Research Fund Denmark through the 'Multi-scale Atmospheric Modeling Above the Seas' (MAMAS) project. This work is also partly funded by the Ministry of Foreign Affairs of Denmark and administered by Danida Fellowship Centre through the 'Multi-scale and model-chain Evaluation of Wind Atlases' (MEWA) project. JDM's contribution is supported by LLNL, United States under contract DE-AC52-07NA27344 and by the US Department of Energy's Wind Energy Technologies Office. We would like to thank the three reviewers for their insightful comments and efforts towards improving our manuscript.

References

[1] Fernández-González S, Martín ML, García-Ortega E, Merino A, Lorenzana J, Sánchez JL, et al. Sensitivity analysis of the WRF model: Wind-resource assessment for complex terrain. J Appl Meteor Climat 2018;57:733–53.

[2] Dörenkämper M, Olsen BT, Witha B, Hahmann AN, Davis NN, Barcons J, et al. The making of the new European wind Atlas – Part 2: Production and evaluation. Geosci Model Dev 2020;13:5079–102.

[3] Gross M, Magar V, Peña A. The effect of averaging, sampling, and time series length on wind power density estimations. Sustainability 2020;12:3431.

[4] IEC. IEC 61400-1. Wind turbines – Part 1: Design guidelines. International Standards, Geneva, Switzerland: International Electrotechnical Commission; 2019.

[5] Conti D, Pettas V, Dimitrov N, Peña A. Wind turbine load validation in wakes using field reconstruction techniques and nacelle LiDAR wind retrievals. Wind Energ Sci 2021;6:841–66.

[6] Skamarock WC, Klemp JB, Dudhia J, Gill DO, Liu Z, Berner J, et al. A description of the advanced research WRF version 4. Technical Report NCAR/TN-556+STR, National Center for Atmospheric Research, Boulder, Colorado, USA; 2019, p. 145 pp.

[7] Kosović B. Subgrid-scale modelling for the large-eddy simulation of high-Reynolds-number boundary layers. J Fluid Mech 1997;336:151–82.

[8] Mirocha JD, Lundquist JK, Kosović B. Implementation of a nonlinear subfilter turbulence stress model for large-eddy simulation in the advanced research WRF model. Mon Wea Rev 2010;138:4212–28.

[9] Muñoz-Esparza D, Lundquist JK, Sauer JA, Kosović B, Linn RR. Coupled mesoscale-LES modeling of a diurnal cycle during the CWEX-13 field campaign: From weather to boundary-layer eddies. J Adv Model Earth Syst 2017;9:1572–94.

[10] Wise AS, Neher JMT, Arthur RS, Mirocha JD, Lundquist JK, Chow FK. Meso- to microscale modeling of atmospheric stability effects on wind turbine wake behavior in complex terrain. Wind Energ Sci 2022;7:367–86.

[11] Arthur RS, Mirocha JD, Marjanovic N, Hirth BD, Schroeder JL, Wharthon S, et al. Multi-scale simulation of wind farm performance during a frontal passage. Atmosphere 2020;11:245.

[12] Peña A, Santos P. Lidar observations and numerical simulations of an atmospheric hydraulic jump and mountain waves. J Geophys Res: Atmos 2021;126. e2020JD033744.

[13] Peña A, Kosović B, Mirocha JD. Evaluation of idealized large-eddy simulations performed with the Weather Research and Forecasting model using turbulence measurements from a 250-m meteorological mast. Wind Energ Sci 2021;6:645–61.

[14] Peña A, Mirocha JD, van der Laan MP. Evaluation of the fitch wind-farm wake parametrization with large-eddy simulations of wakes using the Weather Research and Forecasing model. Mon Wea Rev 2022;150:3051–64.

[15] Schalkwijk J, Jonker HJJ, Siebesma AP, Bosveld FC. A year-long large-eddy simulation of the weather over Cabauw: An overview. Mon Wea Rev 2015;143:828–44.

[16] GmbH M. Flow distortion correction for 3-D flows as measured by METEK's ultrasonic anemometer USA-1. 2004.

[17] Peña A, Dellwik E, Mann J. A method to assess the accuracy of sonic anemometer measurements. Atmos Meas Tech 2019;12:237–52.

[18] Peña A. Østerild: A natural laboratory for atmospheric turbulence. J Renew Sustain Energ 2019;11:063302.

[19] C3S. ERA5: Fifth generation of ECMWF atmospheric reanalyses of the global climate. Copernicus climate change service climate data store (CDS). 2018, https://cds.climate.copernicus.eu/. [Accessed: 17 September 2019].

[20] Donlon CJ, Martin M, Stark JD, Roberts-Jones J, Fiedler E, Wimmer W. The operational sea surface temperature and sea ice analysis (OSTIA) system. Remote Sens Environ 2012;116:140–58.

[21] Danielson JJ, Gesch DB. Global multi-resolution terrain elevation data 2010 (GMTED2010). Technical Report 2011–1073, US Geological Survey; 2011.

[22] Hong S-Y, Dudhia J, Chen S-H. A revised approach to ice microphysical processes for the bulk parameterization of clouds and precipitation. Mon Wea Rev 2004;132:103–20.

[23] Kain J. The Kain–Fritsch convective parameterization: An update. J Appl Meteor Climat 2004;43:170–81.

[24] Nakanishi M, Niino H. Development of an improved turbulence closure model for the atmospheric boundary layer. J Meteorol Soc Japan 2009;87:895–912.

[25] Deardorff JW. Stratocumulus-capped mixed layers derived from a three-dimensional model. Boundary-Layer Meteorol 1980;18:495–527.

[26] Tewari M, Chen F, Wang W, Dudhia J, LeMone MA, Mitchell K, et al. Implementation and verification of the unified noah land surface model in the WRF model. In: 20th conference on weather analysis and forecasting/16th conference on numerical weather prediction. Seattle; 2004.

[27] Iacono MJ, Delamere JS, Mlawer EJ, Shephard MW, Clough SA, Collins WD. Radiative forcing by long-lived greenhouse gases: Calculations with the AER radiative transfer models. J Geophys Res 2008;113:D13103.

[28] Hahmann AN, Sī le T, Witha B, Davis NN, Dörenkämper M, Ezber Y, et al. The making of the New European Wind Atlas – Part 1: Model sensitivity. Geosci Model Dev 2020;13:5053–78.

[29] Vincent CL, Hahmann AN. The impact of grid and spectral nudging on the variance of the near-surface wind speed. J Appl Meteor Climat 2015;54:1021–38.

[30] Knievel JC, Bryan GH, Hacker JP. Explicit numerical diffusion in the WRF model. Mon Wea Rev 2007;135:3808–24.

[31] Technical University of Denmark. Sophia HPC Cluster. 2019, http://dx.doi.org/10.57940/FAFC-6M81, Research Computing at DTU.

[32] Muñoz-Esparza D, Kosović B, van Beeck J, Mirocha J. A stochastic perturbation method to generate inflow turbulence in large-eddy simulation models: Application to neutrally stratified atmospheric boundary layers. Phys Fluids 2015;27:035102.

[33] Muñoz-Esparza D, Kosović B. Generation of inflow turbulence in large-eddy simulations of nonneutral atmospheric boundary layers with the cell perturbation method. Mon Wea Rev 2018;146:1889–909.

[34] Maronga B, Knigge C, Raasch S. An improved surface boundary conditions for large-eddy simulations based on monin-obukhov similarity theory: Evaluation and consequences for grid convergence in neutral and stable conditions. Boundary-Layer Meteorol 2020;174:297–325.

[35] Liu H, Peters G, Foken T. New equations for sonic temperature variance and buoyancy heat flux with an omnidirectional sonic anemometer. Boundary-Layer Meteorol 2001;100:459–68.

[36] Emeis S. Current issues in wind energy meteorology. Meteorol Appl 2014;21:803–19.

[37] Skamarock WC. Evaluating mesoscale NWP models using kinetic energy spectra. Mon Weather Rev 2004;132:3019–32.

[38] Floors R, Enevoldsen P, Davis N, Arnqvist J, Dellwik E. From LiDAR scans to roughness maps for wind resource modelling in forested areas. Wind Energ Sci 2018;3:353–70.

[39] Palma JMLM, Silva CAM, Gomes VC, Silva Lopes A, Simões T, Costa P, et al. The digital terrain model in the computational modelling of the flow over the Perdigão site: The appropriate grid size. Wind Energ Sci 2020;5:1469–85.

[40] Mann J. The spatial structure of neutral atmospheric surface-layer turbulence. J Fluid Mech 1994;273:141–68.

[41] Angevine WM, Olson J, Gristey JJ, Glenn I, Feingold G, Turner DD. Scale awareness, resolved circulations, and practical limits in the MYNN–EDMF boundary layer and shallow cumulus scheme. Mon Wea Rev 2020;148:4629–39.

[42] Juliano TW, Kosović B, Jiménez PA, Eghdami M, Haupt SE, Martilli A. "Gray zone" simulations using a three-dimensional planetary boundary layer parameterization in the Weather Research and Forecasting model. Mon Wea Rev 2022;150:1585–619.

[43] Peña A. Dataset and input files for "One-year-long turbulence measurements and modeling using large-eddy simulation domains in the Weather Research and Forecasting model", Technical University of Denmark. Dataset. 2024. https://doi.org/10.11583/DTU.23763819.v1.